The Astrophysical Journal Supplement Series, 276:71 (14pp), 2025 February https://doi.org/10.3847/1538-4365/ada605

Testing General Relativity Using Large-scale Structure Photometric Redshift Surveys and the Cosmic Microwave Background Lensing Effect

Shang Li[1,2] and Jun-Qing Xia[1,2]
[1] School of Physics and Astronomy, Beijing Normal University, Beijing 100875, People's Republic of China; xiajq@bnu.edu.cn
[2] Institute for Frontiers in Astronomy and Astrophysics, Beijing Normal University, Beijing 100875, People's Republic of China
Received 2024 October 20; revised 2024 December 29; accepted 2025 January 2; published 2025 February 6

Abstract

The E_G statistic provides a valuable tool for evaluating the predictions of general relativity (GR) by probing the relationship between gravitational potential and galaxy clustering on cosmological scales within the observable Universe. In this study, we constrain the E_G statistic using photometric redshift data from the Dark Energy Survey (DES) MagLim sample in combination with the Planck 2018 cosmic microwave background (CMB) lensing map. Unlike spectroscopic redshift surveys, photometric redshift measurements are subject to significant redshift uncertainties, making it challenging to constrain the redshift distortion parameter β with high precision. We adopt a new definition for this parameter, $\beta(z) = f\sigma_8(z)/b\sigma_8(z)$. In this formulation, we reconstruct the growth rate of structure, $f\sigma_8(z)$, using the artificial neural network method, while simultaneously utilizing model-independent constraints on the parameter $b\sigma_8(z)$, directly obtained from the DES collaboration. After obtaining the angular power spectra C_ℓ^{gg} (galaxy–galaxy) and $C_\ell^{g\kappa}$ (galaxy–CMB lensing) from the combination of DES photometric data and Planck lensing, we derive new measurements of the E_G statistic: $E_G = 0.354 \pm 0.146$, 0.452 ± 0.092, 0.414 ± 0.069, and 0.296 ± 0.069 (68% confidence limit) across four redshift bins $z = 0.30$, 0.47, 0.63, and 0.80, respectively, which are consistent with the predictions of the standard Lambda cold dark matter model. Finally, we forecast the E_G statistic using future photometric redshift data from the China Space Station Telescope, combined with lensing measurements from the CMB-S4 project, indicating an achievable constraint on E_G of approximately 1%, improving the precision of tests for GR on cosmological scales.

Unified Astronomy Thesaurus concepts: Large-scale structure of the universe (902); Weak gravitational lensing (1797); Cosmic microwave background radiation (322); Observational cosmology (1146)

1. Introduction

Since the discovery of the accelerated expansion of the Universe through supernova observations, many cosmological and gravitational theories have emerged to explain this phenomenon. One of the most well-known models is the Lambda cold dark matter (ΛCDM) model, often called the standard model of cosmology. This model is popular because of its simplicity and its success in explaining various types of data, including observations of the cosmic microwave background (CMB) and galaxy surveys.

The ΛCDM model assumes that general relativity (GR) is the correct theory of gravity. To account for the accelerated expansion of the Universe, it introduces a constant called Λ, which represents dark energy. This constant creates a type of negative pressure that drives the Universe's expansion to speed up. Interestingly, this constant is mathematically identical to what is expected from quantum vacuum energy, but the problem is that its value, which corresponds to an energy scale of about 10^{-3} eV, is vastly different from the predictions made by particle physics. This discrepancy is one of the biggest mysteries in cosmology.

On the other hand, alternative theories known as modified gravity (MG) models have been developed. These models offer different explanations for the Universe's expansion. Some of them can reproduce the same expansion history as the ΛCDM model without the need for dark energy, which leads to questioning whether GR is the correct theory of gravity at very large (cosmological) scales.

Although GR and MG models may predict similar rates of expansion when considering the Universe as a whole (the "background level"), they usually show differences when we study small variations, or perturbations, in the Universe. These differences can be important for understanding the behavior of cosmic structures, such as galaxies and galaxy clusters, which can help distinguish between these competing theories.

P. Zhang et al. (2007) introduced an elegant statistic, E_G, designed to distinguish between the ΛCDM + GR framework and MG theories. The E_G statistic is defined as the ratio of the Laplacian of the difference between the two scalar potentials, $\nabla^2(\Psi + \Phi)$, to the peculiar velocity divergence field, θ. In practical applications, $\nabla^2(\Psi + \Phi)$ is typically obtained from the cross correlation between gravitational lensing and galaxy clustering, while the peculiar velocity field is derived from the galaxy–velocity cross correlation or, equivalently, from the product of the galaxy autocorrelation and the redshift-space distortion (RSD) parameter $\beta = f/b$, where f is the growth rate of structure and b is the galaxy bias.

Importantly, E_G exhibits scale-dependent behavior under MG models, while it remains scale independent within the ΛCDM framework, as demonstrated by P. Zhang et al. (2007) and A. R. Pullen et al. (2015). This scale dependence makes E_G a powerful tool for directly testing GR. Moreover, a key advantage of the E_G statistic is that it does not depend on galaxy bias or the amplitude of matter perturbations, providing a more robust probe of gravity on cosmological scales.

The first measurement of the E_G statistic was conducted by R. Reyes et al. (2010), using weak-lensing measurements of background galaxies as tracers of gravitational lensing. They obtained $E_G = 0.39 \pm 0.06$ at $z = 0.32$, confirming the predictions of the ΛCDM model on scales ranging from 10 to 50 h^{-1} Mpc. Building on this approach, subsequent measurements of E_G have been extended to larger scales, approximately 70 h^{-1} Mpc, and over redshifts in the range $0.2 \leqslant z \leqslant 0.6$ (C. Blake et al. 2016; S. Alam et al. 2017a; S. De La Torre et al 2017; A. Amon et al. 2018; C. Blake et al. 2020).

In addition, A. R. Pullen et al. (2015) proposed using CMB lensing as an alternative probe for gravitational lensing, enabling E_G to be measured at earlier cosmic times and on larger scales. CMB lensing presents several advantages over galaxy–galaxy lensing. In galaxy–galaxy lensing, source galaxies are typically assigned photometric redshifts, which suffer from significant uncertainties, and are influenced only by foreground galaxies at lower redshifts. In contrast, CMB lensing is sourced at $z = 1100$, which is far enough to be unaffected by galaxy positions at redshifts $z \sim 1$. Moreover, CMB lensing is largely free from complex astrophysical effects, such as intrinsic alignments that can bias galaxy-lensing measurements, due to the nearly Gaussian intrinsic distribution of CMB photons. This makes CMB lensing a more robust and reliable probe for large-scale gravitational lensing effects.

In a recent study, Y. Zhang et al. (2021) estimated the E_G statistic at an effective redshift of $z \sim 1.5$ over scales of 19–190 h^{-1} Mpc, using the Planck 2018 CMB-lensing convergence map (N. Aghanim et al. 2020) and the Sloan Digital Sky Survey (SDSS) eBOSS DR16 quasar clustering catalogs (B. W. Lyke et al. 2020). The results of this analysis were consistent with the predictions of the ΛCDM + GR model within 1σ significance.

To estimate E_G, in addition to gravitational-lensing measurements, it is necessary to measure the growth of structure, which is typically achieved through 3D clustering analysis. This process requires accurate redshift information for tracers, making spectroscopic redshift surveys the preferred method. For photometric redshift surveys, which suffer from lower redshift accuracy, T. Giannantonio et al. (2016) proposed an alternative statistic, D_G, which does not require direct measurements of structure growth. However, D_G requires external information on the galaxy bias, which prevents it from directly distinguishing between GR and MG theories, thereby limiting its utility as a probe for testing gravity at cosmological scales (Omori et al. 2019; Marques & Bernui 2020).

In this work, we aim to estimate the E_G statistic using the magnitude-limited (MagLim) sample from the Dark Energy Survey (DES; B. Flaugher et al. 2015) and the Planck 2018 CMB-lensing data (N. Aghanim et al. 2020). To mitigate the impact of inaccuracies in photometric redshift information on the measurement of structure growth, we calculate the effective redshift of the data set. We then employ the artificial neural network (ANN) method to estimate the corresponding structure growth, utilizing prior measurements derived from spectroscopic data. Additionally, we incorporate model-independent constraints on the parameter $b\sigma_8(z)$, which are directly obtained from the 3×2 pt analysis of the DES galaxy clustering and lensing probes. This approach helps to reduce the errors introduced by photometric redshift uncertainties, thereby improving the reliability of our E_G estimation.

The structure of this paper is organized as follows: In Section 2, we review the theory behind the E_G statistic and the estimator used in our analysis. Section 3 outlines the data sets employed for this study. In Section 4, we detail the methods used to estimate the RSD parameter, the angular power spectrum and covariance matrix, and present the results obtained from real data. Section 5 provides the forecast results for the upcoming galaxy survey, the China Space Station Telescope (CSST). Finally, we summarize our findings and conclusions in Section 6.

For the self-consistency test across all data sets, we assume the following cosmological parameters: $\Omega_m = 0.336$, $\Omega_b = 0.045$, $h = 0.670$, $n_s = 0.959$, and $\sigma_8 = 0.746$, as given in T. Abbott et al. (2023).

2. Formalism and Estimator

2.1. E_G Formalism

We assume a flat ΛCDM Universe described by a perturbed Friedmann–Robertson–Walker metric and consider only scalar perturbations. The metric in the conformal Newtonian gauge is expressed as

$$ds^2 = a(\tau)[-(1 + 2\Psi)d\tau^2 + (1 - 2\Phi)dx^2], \quad (1)$$

where Ψ and Φ represent the weak-field potentials in the time and space metric components, respectively. In GR, when anisotropic stress is negligible, the two potentials are equal, i.e., $\Phi = \Psi$. However, this equality typically does not hold in MG models, leading to a phenomenon known as gravitational slip.

Following P. Zhang et al. (2007), the E_G statistic in Fourier space can be defined as

$$E_G(z, k) = \frac{c^2k^2(\Psi + \Phi)}{3H_0^2(1 + z)\theta(k)}, \quad (2)$$

where $\theta = \nabla \cdot \boldsymbol{v}/H(z)$ is the divergence of the peculiar velocity field $\boldsymbol{v}$, and $H(z)$ is the Hubble expansion rate at redshift z. In linear perturbation theory, $\theta(k)$ can be expressed as $\theta = -f(z)\delta_m(k, z)$, where f is the linear growth rate, which in GR is given by $f \approx [\Omega_m(z)]^{0.55}$. Here, $\Omega_m(z)$ represents the matter density parameter at redshift z.

According to the Poisson equation, $k^2\Phi = \frac{3}{2}H_0^2\Omega_{m0}(1 + z)\delta_m$, and assuming the relation $\Phi = \Psi$, we can simplify the E_G statistic in GR as follows: $E_G(z) = \Omega_{m0}/f(z)$. Under these assumptions, the E_G statistic becomes independent of scale, meaning that it remains constant at a given redshift in GR. In contrast, in MG models, the E_G statistic typically exhibits scale dependence. This scale dependence in MG models arises from deviations in the relationship between the gravitational potentials Ψ and Φ. Consequently, measuring E_G at different scales could distinguishing between GR and alternative theories of gravity.

Following Equation (2), the E_G statistic can also be expressed in terms of power spectra as

$$E_G(k, z) = \frac{c^2P_{\nabla^2(\Psi+\Phi)g}(k)}{3H_0^2(1 + z)P_{\theta g}(k)}, \quad (3)$$

where $P_{\nabla^2(\Psi+\Phi)g}$ is the galaxy–$\nabla^2(\Psi + \Phi)$ cross-power spectrum and $P_{\theta g}$ is the galaxy–peculiar velocity cross-power spectrum. By projecting the 3D power spectrum onto a 2D

spherical surface, E_G can be estimated as

$$E_G(\ell, \bar{z}) = \frac{c^2 C_\ell^{g\kappa}}{3H_0^2 C_\ell^{g\theta}}, \tag{4}$$

where $\bar{z}$ is the effective redshift of the galaxy survey, $C_\ell^{g\kappa}$ is the measured lensing convergence–galaxy cross-correlation angular power spectrum, and $C_\ell^{g\theta}$ is the velocity–galaxy cross-correlation angular power spectrum.

In practice, measuring $C_\ell^{g\theta}$ directly is challenging. However, we can utilize the relationship $C_\ell^{g\theta} = C_\ell^{gg} \cdot \beta$, where $\beta = f/b$ is the RSD parameter and b is the linear bias parameter of the galaxy survey. This allows us to replace $C_\ell^{g\theta}$ with the product of the galaxy autocorrelation power spectrum C_ℓ^{gg} and β, which are easier to measure. Then, the modified expression for E_G becomes (A. R. Pullen et al. 2015)

$$E_G(\ell, \bar{z}) = \Gamma(\bar{z}) \frac{C_\ell^{g\kappa}}{\beta(\bar{z}) C_\ell^{gg}}, \tag{5}$$

where $\Gamma(z)$ is the calibration factor.

2.2. Angular Power Spectrum

In the Limber approximation, the angular cross-correlation power spectrum between two tracers can be described generally as (D. N. Limber 1953)

$$C_\ell^{XY} = \int dz \, \frac{H(z)}{c} \, \frac{W_X(z) W_Y(z)}{\chi^2(z)} \, P_{XY}\left(\frac{\ell + 1/2}{\chi(z)}, z\right), \tag{6}$$

where $\chi(z)$ is the comoving distance at redshift z, $W_{X/Y}(z)$ are the window functions for the respective tracers, c is the speed of light, and P_{XY} is the 3D power spectrum of the two tracers. In the estimation of the E_G statistic, we mainly focus on the linear regime. Therefore, we can substitute the matter power spectrum $P_{mm}(k, z)$ in place of $P_{XY}(k, z)$, since linear matter fluctuations dominate at large scales. The tracer-specific effects are then incorporated into the window functions.

For the galaxy survey, the window function is given by $W_g(z) = b(z)n(z)$, where $b(z)$ is the galaxy bias and $n(z)$ is the redshift distribution of the galaxy sample. The lensing convergence window function for the CMB at redshift $z_* = 1100$ is expressed as

$$W_\kappa(z, z_*) = \frac{3H_0^2 \Omega_{m,0}}{2cH(z)}(1 + z) W(z, z_*), \tag{7}$$

where the lensing convergence kernel function $W(z, z_*)$ is given by

$$W(z, z_*) = \chi(z)\left(1 - \frac{\chi(z)}{\chi(z_*)}\right), \tag{8}$$

with $\chi(z)$ being the comoving distance at redshift z, and $\chi(z_*)$ is the comoving distance to the CMB. Using these window functions, the angular power spectra C_ℓ^{gg} and $C_\ell^{g\kappa}$ can be described as

$$C_\ell^{gg} = \int dz \frac{H(z)}{c} \left[\frac{b(z)n(z)}{\chi(z)}\right]^2 P_{mm}\left(\frac{\ell + 1/2}{\chi(z)}, z\right), \tag{9}$$

and

$$C_\ell^{g\kappa} = \frac{3H_0^2 \Omega_{m,0}}{2c^2} \int dz (1 + z) \frac{W(z, z_*)}{\chi^2(z)} \times b(z)n(z) P_{mm}\left(\frac{\ell + 1/2}{\chi(z)}, z\right). \tag{10}$$

These expressions provide the theoretical predictions for the galaxy autocorrelation power spectrum and the galaxy–CMB lensing cross-correlation power spectrum.

2.3. Calibration Factor

In addition to the angular power spectra C_ℓ^{gg} and $C_\ell^{g\kappa}$, a calibration factor $\Gamma(z)$ is needed for estimating E_G in Equation (5). Following A. R. Pullen et al. (2016) and S. Yang & A. R. Pullen (2018), in the calibration factor $\Gamma(z)$ it is essential to consider several additional factors beyond the standard normalization term to ensure accuracy

$$\Gamma(\ell, z) = C_\Gamma C_b \frac{2c}{3H_0}\left[\frac{H(z)n(z)}{H_0(1 + z)W(z, z_*)}\right], \tag{11}$$

where C_Γ and C_b are extra calibration factors that account for the broad redshift distribution and the lensing kernel, as well as for scale-dependent bias due to nonlinear clustering. These are expressed as

$$C_\Gamma(\ell, z) = \frac{W(z, z_*)(1 + z)}{2n(z)} \frac{c}{H(z)} \frac{C_\ell^{mg}}{Q_\ell^{mg}}, \tag{12}$$

and

$$C_b(\ell, z) = \frac{C_\ell^{gg}}{b(\bar{z}) C_\ell^{mg}}, \tag{13}$$

where C_ℓ^{mg} is the angular power spectrum that combines galaxy bias with the matter power spectrum

$$C_\ell^{mg} = \int_0^\infty dz \frac{H(z)}{c} b(z) n^2(z) \chi^{-2}(z) P_{mm}\left(\frac{\ell + 1/2}{\chi(z)}, z\right), \tag{14}$$

and Q_ℓ^{mg} is given by

$$Q_\ell^{mg} = \frac{1}{2} \int_0^\infty dz W(z, z_*) b(z) n(z) \chi^{-2}(z) \times (1 + z) P_{mm}\left(\frac{\ell + 1/2}{\chi(z)}, z\right). \tag{15}$$

These equations provide the framework to compute the necessary calibration factors $\Gamma(z)$, which are crucial for correcting the estimation of E_G. The calibration accounts for both the impact of galaxy redshift distribution and the effects of nonlinear clustering on bias and lensing.

3. Observational Data

3.1. DES MagLim Sample

The DES (B. Flaugher et al. 2015) is a large-scale imaging survey designed to cover approximately 5000 deg^2 of the southern sky, employing five broadband filters (*grizY*) to observe galaxies. DES operates with a 570 MP camera mounted on the 4 m Blanco

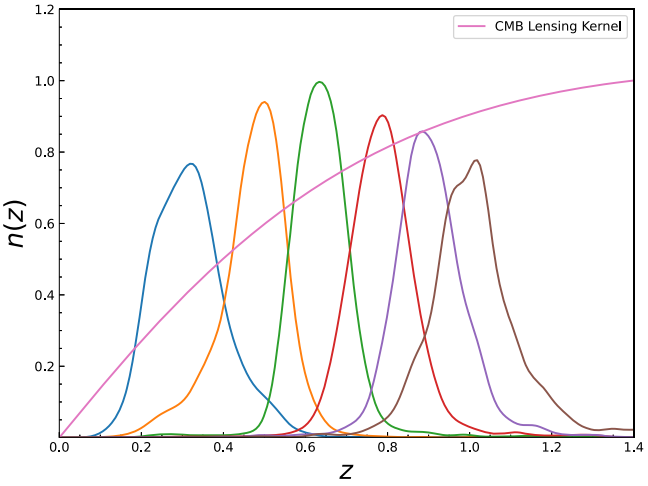

Figure 1. Redshift distributions of the DES Y3 MagLim sample. The kernel function of the CMB lensing is also shown in the figure. For clarity, all results have been normalized.

telescope at the Cerro Tololo Inter-American Observatory in Chile. One of the key scientific goals of DES is to provide stringent constraints on cosmological parameters, including the dark energy equation of state parameter w.

This work utilizes data from the first three years (Y3) of DES observations, collected between 2013 August and 2016 February. The analysis focuses on the MagLim galaxy sample derived from the Y3 GOLD catalog, applying the same selection criteria as M. Rodrìguez-Monroy et al. (2022). The MagLim sample is defined by an i-band magnitude cut that depends linearly on the photometric redshift, facilitating the inclusion of a greater number of higher-redshift galaxies. The photometric redshifts for the MagLim sample are estimated using the directional neighborhood fitting algorithm (J. De Vicente et al. 2016).

In line with the method used by A. Porredon et al. (2022) and J. Sánchez (2022), we divide the MagLim galaxies into six tomographic redshift bins ranging from $z = 0.2$ to $z = 1.05$, with bin edges at [0.20, 0.40, 0.55, 0.70, 0.85, 0.95, 1.05]. Figure 1 shows the redshift distribution for each tomographic bin. However, consistent with the findings of T. M. Abbott et al. (2022), we adopt a conservative approach and exclude the two highest redshift bins from our analysis. This decision stems from issues identified after unblinding the data, where significant discrepancies were observed in both the clustering and galaxy–galaxy lensing signals for galaxies at $z > 0.85$, leading to poor fits with the cosmological models under consideration.

The MagLim catalog assigns a weight to each galaxy to correct for observational systematics, as described in M. Rodrìguez-Monroy et al. (2022). Using these weights, we construct a map of the number of sources per pixel, where the total number of galaxies in pixel p is computed as $N_p = \sum_{i \in p} w_i$, with w_i being the weight of the ith galaxy. For the pixelization scheme, we choose the HEALPix resolution parameter $N_{\rm side} = 2048$, which matches the resolution of the CMB-lensing mask map discussed in Section 3.2.

Each pixel in the galaxy overdensity map is then defined by the relation (G. Marques et al. 2024)

$$\delta_p = \left(\frac{1}{f_p} \frac{N_p}{\bar{n}} \right) - 1, \tag{16}$$

where $\bar{n}$ represents the mean number of sources in the unmasked pixels and is calculated as

$$\bar{n} = \frac{\sum_p N_p}{\sum_p f_p}. \tag{17}$$

Here, f_p denotes the fractional coverage of each pixel, which accounts for the DES mask. The DES mask is provided at a higher resolution of $N_{\rm side} = 4096$, with values of f_p ranging from 0.8 to 1 for effectively observed regions. To match the galaxy map resolution, we average the f_p values from the higher-resolution pixels, degrading the mask map to $N_{\rm side} = 2048$.

Following this processing, we obtain a galaxy density map and the corresponding mask map, which together cover an area of 4143 deg^2 of the sky. These maps will be used for the galaxy clustering analysis in this work.

3.2. Cosmic Microwave Background Lensing

Gravitational lensing of the CMB can be detected, due to detailed understanding of the primordial CMB's statistical properties. As CMB photons travel from the last scattering surface to Earth, their paths are deflected by intervening matter, causing subtle distortions in the observed anisotropies. These distortions alter the statistical characteristics of the CMB, enabling the reconstruction of a map of the gravitational potential responsible for the deflection. This gravitational potential provides valuable insights into the growth and distribution of cosmic structures.

Since the CMB-lensing map traces the matter distribution directly, it acts as an unbiased tracer of the Universe's matter density field. For this analysis, we use the minimum-variance (MV) estimate of the gravitational lensing convergence, as reconstructed from the CMB temperature and polarization measurements in the Planck 2018 data release (N. Aghanim et al. 2020).

Specifically, we utilize the `COM_Lensing_4096_R3.00` data set, which is based on both temperature and polarization measurements. This data set comes with a survey mask covering approximately 70% of the sky at $N_{\rm side} = 2048$ and includes the noise estimate for the Planck lensing reconstruction, $N_\ell^{\kappa\kappa}$. The MV lensing potential estimates are derived from SMICA DX12 CMB maps, with the lensing convergence available in spherical harmonics coefficients, $a_{\ell m}$, up to $\ell_{\rm max} = 4096$.

For our analysis, we limit the range of multipoles to $8 \leqslant \ell \leqslant 2048$, excluding higher multipoles due to the significant reconstruction noise at small scales. This choice focuses on quasi-linear scales, where the contribution from nonlinear effects is minimal relative to statistical errors. Moreover, we adopt a conservative multipole range of $\ell_{\rm min} = 80$ and $\ell_{\rm max} = 400$, as we will discuss in more detail in Section 4, to ensure that nonlinear scales do not dominate our results.

4. Numerical Results

4.1. Redshift-space Distortion Parameter

In cosmological analyses, the growth of structure is typically measured through 3D clustering, which necessitates precise redshift information for tracers. As such, spectroscopic redshift surveys are generally preferred due to their superior accuracy,

Table 1
The $\hat{f}$ Data Compilation Used in the Analysis

z	$\hat{f}$	Reference	z	$\hat{f}$	Reference	z	$\hat{f}$	Reference
0.35	0.440 ± 0.050	[1a]	0.77	0.490 ± 0.18	[1b]	0.17	0.510 ± 0.060	[1c]
0.02	0.314 ± 0.048	[2], [3a]	0.02	0.398 ± 0.065	[3b], [4]	0.25	0.3512 ± 0.0583	[5]
0.37	0.4602 ± 0.0378	[5]	0.25	0.3665 ± 0.0601	[5]	0.37	0.4031 ± 0.0586	[5]
0.44	0.413 ± 0.080	[6]	0.60	0.390 ± 0.063	[6]	0.73	0.437 ± 0.072	[6]
0.067	0.423 ± 0.055	[7]	0.30	0.407 ± 0.055	[8]	0.40	0.419 ± 0.041	[8]
0.50	0.427 ± 0.043	[8]	0.60	0.433 ± 0.067	[8]	0.80	0.470 ± 0.080	[9]
0.35	0.429 ± 0.089	[10]	0.18	0.360 ± 0.090	[11]	0.38	0.440 ± 0.060	[11]
0.32	0.384 ± 0.095	[12a]	0.32	0.48 ± 0.10	[12b]	0.57	0.417 ± 0.045	[12b]
0.15	0.490 ± 0.145	[13]	0.10	0.370 ± 0.130	[14]	1.40	0.482 ± 0.116	[15]
0.59	0.488 ± 0.060	[16]	0.38	0.497 ± 0.045	[17]	0.51	0.458 ± 0.038	[17]
0.61	0.436 ± 0.034	[17]	0.38	0.477 ± 0.051	[18]	0.51	0.453 ± 0.050	[18]
0.61	0.410 ± 0.044	[18]	0.76	0.440 ± 0.040	[19]	1.05	0.280 ± 0.080	[19]
0.32	0.427 ± 0.056	[20]	0.57	0.426 ± 0.029	[20]	0.727	0.296 ± 0.0765	[21]
0.02	0.428 ± 0.0465	[22]	0.60	0.550 ± 0.120	[23]	0.86	0.400 ± 0.110	[23]
0.1	0.48 ± 0.16	[24]	0.001	0.505 ± 0.085	[25]	0.85	0.45 ± 0.11	[26]
0.31	0.384 ± 0.083	[27]	0.36	0.409 ± 0.098	[27]	0.40	0.461 ± 0.086	[27]
0.44	0.426 ± 0.062	[27]	0.48	0.458 ± 0.063	[27]	0.52	0.483 ± 0.075	[27]
0.56	0.472 ± 0.063	[27]	0.59	0.452 ± 0.061	[27]	0.64	0.379 ± 0.054	[27]
0.1	0.376 ± 0.038	[28]	1.52	0.420 ± 0.076	[29]	1.52	0.396 ± 0.079	[30]
0.978	0.379 ± 0.176	[31]	1.23	0.385 ± 0.099	[31]	1.526	0.342 ± 0.070	[31]
1.944	0.364 ± 0.106	[31]	0.60	0.49 ± 0.12	[32]	0.86	0.46 ± 0.09	[32]
0.57	0.501 ± 0.051	[33]	0.03	0.404 ± 0.0815	[34]	0.72	0.454 ± 0.139	[35]

Note. References: (1a) SDSS-LRG, (1b) VVDS, and (1c) 2dFGRS (Y.-S. Song & W. J. Percival 2009); (2) 2MRS (M. Davis et al. 2011); (3a) 2MRS and (3b) Type Ia supernova (SN Ia) + IRAS (M. J. Hudson & S. J. Turnbull 2012); (4) SN Ia + IRAS (S. J. Turnbull et al. 2012); (5) SDSS-LRG-200 (L. Samushia et al. 2012); (6) WiggleZ (C. Blake et al. 2012); (7) 6dFGS (F. Beutler et al. 2012); (8) SDSS-BOSS (R. Tojeiro et al. 2012); (9) VIPERS (S. De La Torre et al. 2013); (10) SDSS-DR7-LRG (C.-H. Chuang & Y. Wang 2013); (11) GAMA (C. Blake et al. 2013); (12a) BOSS-LOWZ and (12b) SDSS DR10 and DR11 (A. G. Sánchez et al. 2014); (13) SDSS-MGS (C. Howlett et al. 2015); (14) SDSS-veloc (M. Feix et al. 2015); (15) FastSound (T. Okumura et al. 2016); (16) SDSS-CMASS (C.-H. Chuang et al. 2016); (17) BOSS DR12 (S. Alam et al. 2017b); (18) BOSS DR12 (F. Beutler et al. 2017); (19) VIPERS v7 (M. J. W.lson 2016); (20) BOSS-LOWZ (H. Gil-Marìn et al. 2017); (21) VIPERS (A. Hawken et al. 2017); (22) 6dFGS + SN Ia (D. Huterer et al. 2017); (23) VIPERS PDR2 (A. Pezzotta et al. 2017); (24) SDSS DR13 (M. Feix et al. 2017); (25) 2MTF (C. Howlett et al. 2017); (26) VIPERS PDR2 (F. Mohammad et al. 2018a); (27) BOSS DR12 (Y. Wang et al. 2018); (28) SDSS DR7 (F. Shi et al. 2018); (29) SDSS-IV (H. Gil-Marìn et al. 2018); (30) SDSS-IV (J. Hou et al. 2018); (31) SDSS-IV (G.-B. Zhao et al. 2019); (32) VIPERS PDR2 (F. Mohammad et al. 2018b); (33) BOSS DR12 voids (S. Nadathur et al. 2019); (34) 2MTF 6dFGSv (F. Qin et al. 2019); and (35) SDSS-IV (M. Icaza-Lizaola et al. 2020).

whereas photometric redshift surveys, such as DES, suffer from lower redshift precision. Consequently, in our analysis, we do not directly estimate the RSD parameter $\beta = f/b$ from photometric redshift data. Instead, we adopt a modified expression, $\beta(z) = \hat{f}/\hat{b}$, where $\hat{f} = f\sigma_8(z)$ and $\hat{b} = b\sigma_8(z)$ (L. Wenzl et al. 2024). By leveraging the DES galaxy and lensing probes, we can estimate $\hat{b}$, while $\hat{f}$ is derived from previous spectroscopic measurements of the linear growth rate, employing a regression algorithm.

4.1.1. $\hat{f}$ Measurement

First, we provide the complete set of $\hat{f}$ measurements utilized in our analysis in Table 1, which includes 66 $\hat{f}$ measurements from various large-scale structure (LSS) spectroscopic redshift surveys, covering the redshift range from $z = 0.001$ to $z = 1.944$ (L. Kazantzidis & L. Perivolaropoulos 2018; F. Skara & L. Perivolaropoulos 2020).

Subsequently, we employed a fitting approach, ANN fitting, to derive the $\hat{f}$ values for the MagLim sample at their corresponding effective redshifts. Here, we opted for ANN over the more conventional Gaussian process (GP) due to concerns raised in previous studies (L. Perenon et al. 2021), which suggest that the current data's distribution and precision can cause GP reconstructions to be overly sensitive to prior assumptions, such as hyperparameter ranges or mean functions. In contrast, ANN, being a machine learning method, has been demonstrated to be a universal approximator capable of modeling a wide range of functions. It is a purely data-driven technique that does not impose Gaussian assumptions. Thus, with an appropriately chosen network architecture, ANN can provide an accurate representation of the input data's distribution. Therefore, in our analysis, we used the open-source package `ReFANN`[3] (G.-J. Wang et al. 2020) to perform the ANN fitting process.

In Figure 2 we present the estimations of $\hat{f}$ for the MagLim sample at their corresponding effective redshifts. Using these 66 data points, we can determine the evolution of $\hat{f}$ with redshift through the ANN algorithm, as shown by the black solid line in the figure. The light green region represents the 68% confidence interval for the $\hat{f}(z)$ provided by the ANN algorithm, and it is evident that due to the higher density of observational data between redshifts of 0.3 and 0.6, the error in the final reconstruction of $\hat{f}(z)$ is smaller around a redshift of 0.5. By comparing this with the theoretical curve from the ΛCDM model (orange dashed line), we observe that the evolution of $\hat{f}$ derived from the existing data is consistent with that predicted by ΛCDM at 68% confidence level. The final estimations of $\hat{f}$ at four redshifts are listed in Table 2.

[3] https://github.com/Guo-Jian-Wang/refann

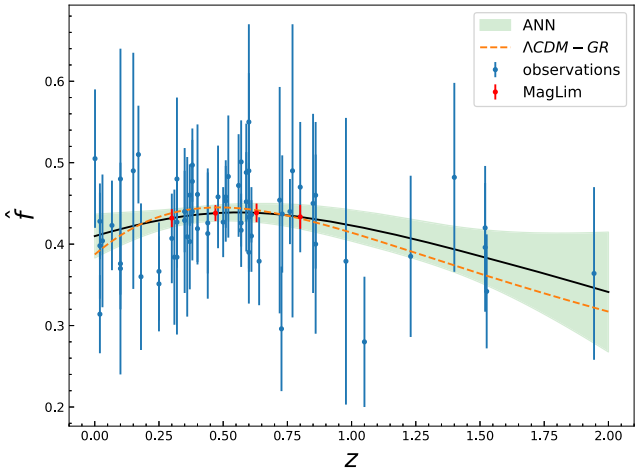

Figure 2. The reconstruction of the function $\hat{f}(z)$ from the $\hat{f}$ measurements, shown as the black solid line, along with the 68% confidence level indicated by the light green region. The blue points with error bars represent the $\hat{f}$ values obtained from the literature, while the red stars denote the inferred $\hat{f}$ values for the DES MagLim sample. For comparison, the theoretical prediction of $\hat{f}(z)$ based on the ΛCDM model is also displayed.

4.1.2. $\hat{b}$ Measurement

We obtain the $\hat{b}$ values for the DES MagLim sample from the data chains provided by T. Abbott et al. (2023).[4] Their analysis used the Y3 observations from DES, either independently or in combination with external cosmological probes, to constrain potential extensions of the ΛCDM model. Specifically, they employed the two-point correlation functions of weak gravitational lensing, galaxy clustering, and their cross correlations (commonly referred to as 3 × 2 pt) to constrain six different extensions of the ΛCDM model.

One of these extensions is a binned $\sigma_8(z)$ model, which serves as a phenomenological probe of structure growth without assuming specific physical mechanisms. In this approach, the binned $\sigma_8(z)$ model is defined as

$$\sigma_8^{[\text{bin } i]} \equiv \sigma_8 \sqrt{A_i^{P_{\text{lin}}}}, \tag{18}$$

where $A_i^{P_{\text{lin}}}$ represents the amplitude of the linear matter power spectrum in the ith redshift bin, which equals 1 in the ΛCDM model. Therefore, we can determine the amplitude of the growth of structure, σ_8, in each redshift bin. Additionally, the numerical chains provide direct access to the linear bias for each redshift bin, enabling us to derive constraints on the combined parameter $\hat{b} = b\sigma_8$. The resulting constraints on $\hat{b}$, obtained from the chains, are presented in Table 2.

In conclusion, we utilize the measurements of $\hat{f}(z)$ and $\hat{b}(z)$ to estimate the RSD parameter $\beta(z)$ for the first four tomographic bins of the DES MagLim sample, with the results detailed in Table 2. To assess the uncertainties in $\beta(z)$, we apply the error propagation method. Notably, the uncertainties in our reconstructed β values are significantly smaller than those obtained from current constraints based on 3D power spectrum analyses. This improvement primarily stems from the reconstructed linear growth rate, which incorporates multiple $\hat{f}$ measurements from various sources rather than relying on a single survey. Moreover, we find that the uncertainties in β have a minimal impact on the subsequent E_G estimates, as the dominant source of error in current E_G estimates arises from uncertainties in the power spectra.

[4] https://desdr-server.ncsa.illinois.edu/despublic/y3a2_files/y3a2_beyond_lcdm/chains/

Table 2
The Effective Redshifts, Corresponding Galaxy Bias $\hat{b} = b\sigma_8(z)$ Values, Linear Growth Rate, and the Calculated $\beta = \hat{f}/\hat{b}$ Values

z_{eff}	$\hat{b} = b\sigma_8(z)$	$\hat{f} = f\sigma_8(z)$	$\beta = \hat{f}/\hat{b}$
0.30	0.924 ± 0.034	0.432 ± 0.011	0.467 ± 0.021
0.47	0.956 ± 0.044	0.438 ± 0.010	0.458 ± 0.023
0.63	1.003 ± 0.035	0.438 ± 0.011	0.437 ± 0.019
0.80	0.865 ± 0.034	0.434 ± 0.015	0.501 ± 0.026

Note. The table shows the effective redshifts of the first four tomographic bins of the DES MagLim sample, along with the corresponding galaxy bias $\hat{b} = b\sigma_8(z)$ values from T. Abbott et al. (2023), the linear growth rate values derived using ReFANN, and the calculated $\beta = \hat{f}/\hat{b}$ values.

4.2. Angular Power Spectrum

We then calculate the angular power spectra C_ℓ^{gg} and $C_\ell^{g\kappa}$ using the galaxy number density map from the DES MagLim sample and the lensing measurements from Planck. These calculations are performed using the pseudo-C_ℓ estimator, implemented in the `NaMaster` software package,[5] which provides an unbiased estimate of the angular power spectra.

The estimation of the angular power spectrum is affected by the survey's sky coverage, as the mask introduces coupling between different modes of the true power spectrum. In this framework, the true underlying power spectrum, C_ℓ^{true}, is derived from the observed power spectrum, C_ℓ^{obs}, by applying the inverse of the mode-coupling matrix, M, as

$$C_\ell^{\text{true}} = \sum_{\ell'} M_{\ell\ell'} C_{\ell'}^{\text{obs}}. \tag{19}$$

The mode-coupling matrix $M_{\ell\ell'}$ is determined entirely by the mask information. As shown in E. Hivon et al. (2002), the coupling matrix $M_{\ell\ell'}$ can be efficiently and analytically computed due to the orthogonality of the Wigner 3j symbols. To mitigate the effects of the mask, we apply a binning process to the resulting power spectrum, using a wide multipole bin width of $\Delta\ell = 30$. This approach helps to reduce the correlations between different multipole bins, ensuring that the impact of mode coupling is minimized and that the correlations among the binned multipoles remain small.

Given the sky coverage of the DES survey and the use of the Limber approximation in our analysis, we apply a conservative cut on large scales by setting the minimum multipole value to $\ell_{\text{min}} = 80$. To address the effects of nonlinearity, we define a maximum wavenumber, k_{nl}, for the transition from linear to quasi-linear scales. This is determined by the condition $k_{\text{nl}}^3 P(k_{\text{nl}}, \bar{z})/(2\pi^2) = 1$, following the approach outlined in S. Yang & A. R. Pullen (2018). Given that the DES photometric data are used, we adopt a more conservative approach by setting an upper limit of $\ell_{\text{max}} < 400$. This results in maximum multipole values of 188, 390, 400, and 400 for the respective MagLim redshift bins used in the E_G estimator. This conservative selection helps to mitigate the impact of

[5] https://github.com/LSSTDESC/NaMaster

nonlinearity and ensures the robustness of the analysis on middle scales.

Furthermore, the observed galaxy autocorrelation power spectrum is affected by the discrete nature of galaxies, which introduces an additional shot-noise contribution. Typically, the galaxy sample is assumed to follow a Poisson distribution, allowing the shot noise to be estimated as (C. Garcìa-Garcìa et al. 2021)

$$N_\ell = \sum_{\ell'} (M^{-1})_{\ell\ell'} \tilde{N}_\ell, \quad \tilde{N}_\ell = \frac{\langle m \rangle}{\bar{n}_{\rm eff}}. \tag{20}$$

Here, $\langle m \rangle$ represents the mean value of the mask across the full sky, and $\bar{n}_{\rm eff}$ denotes the effective mean number density, defined as

$$\bar{n}_{\rm eff} = \frac{\left(\sum_{i\in p} w_i\right)^2}{\Omega_{\rm pix} \sum_p m_p \sum_{i\in p} w_i^2}, \tag{21}$$

where $\Omega_{\rm pix}$ is the pixel area in steradians, m_p is the mask value for pixel p, and w_i is the weight assigned to each galaxy in pixel p.

In our analysis, we subtract the shot-noise contribution from the observed galaxy autocorrelation power spectrum $C_\ell^{\rm gg}$. Afterward, we correct the resulting power spectrum by dividing them by the square of the pixel window function, which is obtained using the standard HEALPix tools. This process ensures that the power spectrum is properly corrected for pixelization effects. For the observed galaxy-lensing convergence power spectrum $C_\ell^{\rm g\kappa}$, since the CMB-lensing convergence κ is a continuous field unaffected by the pixel window function and the pixel window function is not applied in the $a_{\ell m}$ to map transformation, we only need to correct for the pixelization effects by dividing by a single pixel window function.

4.3. Covariance Matrices

In our analysis, we employ the jackknife (JK) resampling method to estimate covariance matrices, relying exclusively on the available data sample.

The overlapping sky region between the DES MagLim sample and the Planck lensing data is partitioned into $N_{\rm JK}$ equal-area patches. JK subsamples are generated by sequentially omitting one patch at a time, resulting in a set of leave-one-out samples. The JK-estimated mean power spectrum across all patches is calculated as

$$\langle X_\ell \rangle = \frac{1}{N_{\rm JK}} \sum_{k=1}^{N_{\rm JK}} X_\ell^{(k)}. \tag{22}$$

The covariance of the measurements is determined by aggregating the variations across all patches. The general expression for the covariance between two angular power spectra, X_ℓ and $Y_{\ell'}$, is given by

$$\boldsymbol{C}(X_\ell, Y_{\ell'}) = \frac{N_{\rm JK} - 1}{N_{\rm JK}} \sum_{k=1}^{N_{\rm JK}} (X_\ell^{(k)} - \langle X_\ell \rangle)(Y_{\ell'}^{(k)} - \langle Y_{\ell'} \rangle), \tag{23}$$

where $X_\ell, Y_\ell \in [C_\ell^{\rm g\kappa}, C_\ell^{\rm gg}]$.

In the case of autocorrelations, it is necessary to account for variations in shot noise within the galaxy map when a patch is removed. As outlined by L. Wenzl et al. (2024), the shot noise in the subsample can be analytically represented as

$$N_\ell^{(k)} = \frac{N_{\rm JK}}{N_{\rm JK} - 1} N_\ell. \tag{24}$$

The number of JK samples is determined by the largest scales we aim to investigate. A. R. Pullen et al. (2015) suggested that the minimum patch size should adequately capture the largest cosmological scales. Adhering to this recommendation, we conservatively select $N_{\rm JK} = 30$ patches for our analysis. We also varied the number of patches $N_{\rm JK}$ to ensure the stability of the covariance matrix.

For a multivariate Gaussian vector with a finite sample size, the estimated covariance matrix $\hat{\boldsymbol{C}}$ follows a Wishart distribution, providing an unbiased estimate of the true covariance matrix $\boldsymbol{C}$. However, the inverse of the estimated covariance matrix, $\hat{\boldsymbol{C}}^{-1}$, which follows an inverse Wishart distribution, is a biased estimate of the true inverse covariance matrix $\boldsymbol{C}^{-1}$. This bias arises from inaccuracies in $\hat{\boldsymbol{C}}$. To address this issue, we follow the approach outlined by J. Hartlap et al. (2007) and apply a correction factor to obtain the unbiased inverse covariance

$$\hat{\boldsymbol{C}}^{-1}_{\rm unbiased} = \left(1 - \frac{N_d + 1}{N_{\rm JK} - 1}\right) \hat{\boldsymbol{C}}^{-1}, \tag{25}$$

where N_d denotes the number of band powers utilized, and its values are 3, 10, 10, and 10 for each redshift bin, respectively. Furthermore, S. Dodelson & M. D. Schneider (2013) emphasized that, in maximum likelihood fitting, the errors in the inverse covariance matrix $\hat{\boldsymbol{C}}^{-1}$ propagate to the model parameters. This effect can be mitigated by multiplying the inverse covariance matrix by the following factor (J. W. Percival et al. 2014)

$$\boldsymbol{M} = \frac{1 + B(N_d - N_p)}{1 + A + B(N_p + 1)}, \tag{26}$$

where N_p represents the number of parameters, and for the estimation of the single parameter E_G, $N_p = 1$. The constants A and B are defined as

$$A = \frac{2}{(N_{\boldsymbol{JK}} - N_d - 1)(N_{\boldsymbol{JK}} - N_d - 4)},$$
$$B = \frac{N_{\boldsymbol{JK}} - N_d - 2}{(N_{\boldsymbol{JK}} - N_d - 1)(N_{\boldsymbol{JK}} - N_d - 4)}. \tag{27}$$

In Figure 3, we present the observed power spectra C_ℓ^{gg} and $C_\ell^{g\kappa}$ derived from the DES MagLim sample and the Planck lensing measurements across the four tomographic redshift bins as well as their ratio, R_ℓ. For illustrative purposes, we include the square roots of the diagonal elements of the JK covariance matrix as 1σ error bars on the data points. Additionally, we indicate the scale cuts, where multipoles larger than the maximum ℓ are excluded, by shading the corresponding regions in gray.

Furthermore, we also conduct a comparison between the observed power spectra C_ℓ^{gg} and $C_\ell^{g\kappa}$ and their corresponding theoretical predictions for each tomographic redshift bin. The theoretical predictions are generated using the DESC Core Cosmology Library (N. E. Chisari et al. 2019), with the underlying 3D power spectra computed via the CAMB Boltzmann code. To ensure consistency between the observed and theoretical power spectra, we apply the appropriate binned

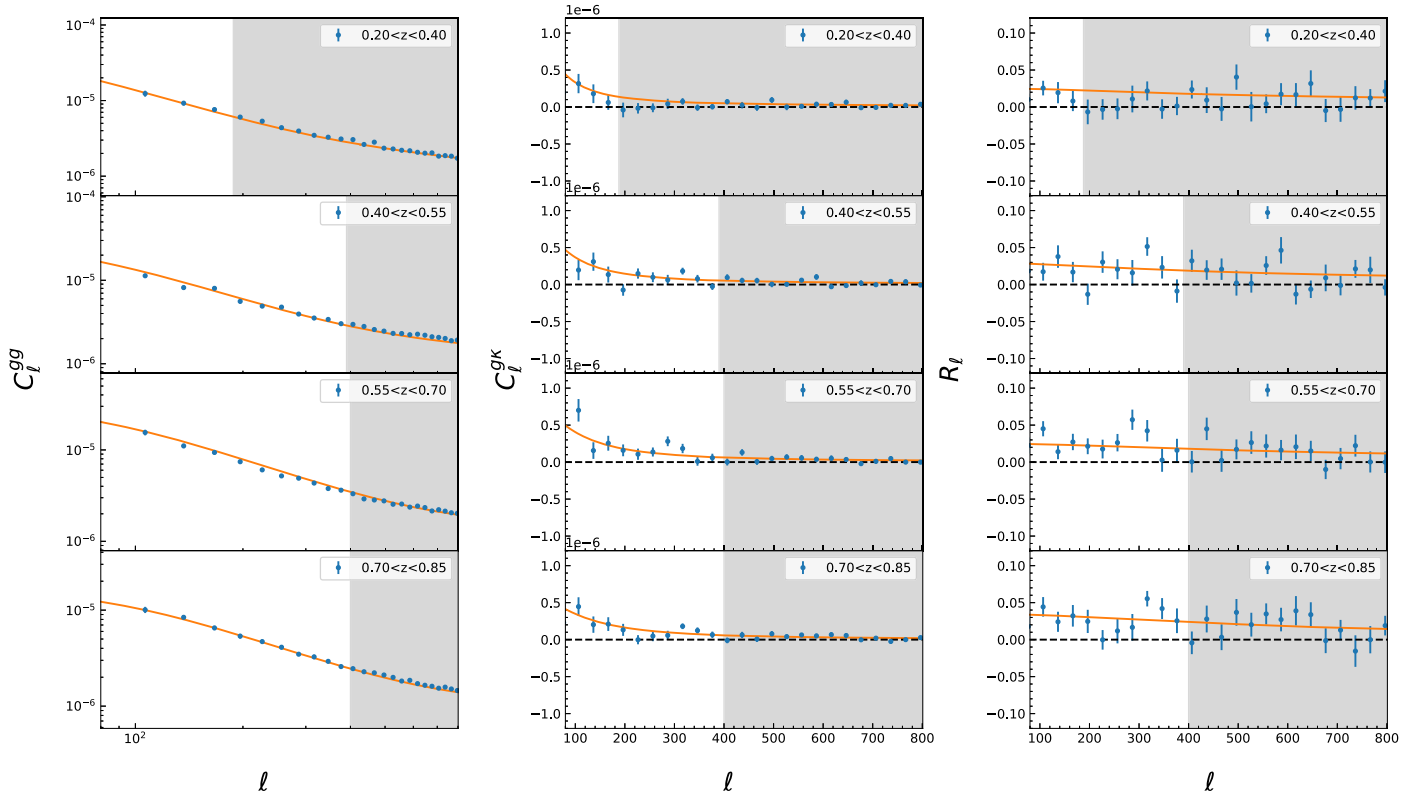

Figure 3. The observed power spectra C_ℓ^{gg} (left panels) and $C_\ell^{g\kappa}$ (middle panels) and their ratio R_ℓ (right panels) for the four redshift bins of the DES MagLim sample are shown. The solid orange lines depict the theoretical predictions evaluated using the best-fit parameters from T. Abbott et al. (2023). The gray-shaded regions highlight the range of multipoles that were excluded from the analysis due to nonlinearity.

mode-coupling matrix and binning scheme to the theoretical curves, accounting for the effects of the survey mask and binning process. For the linear bias in each redshift bin, we adopt the best-fit values derived from the 3 × 2 pt measurements of the DES Y3 observations (T. Abbott et al. 2023), consistent with the values used in Section 4.1.2. The comparison shows that the measurements of both C_ℓ^{gg} and $C_\ell^{g\kappa}$ align well with the theoretical predictions.

4.4. $E_G(\ell)$ Estimation

After obtaining the measurements of the RSD parameter β, along with the angular power spectra C_ℓ^{gg} and $C_\ell^{g\kappa}$, we estimate the E_G statistic as a function of the multipole using Equation (5), as presented in Figure 4. Due to the maximum multipole for the first redshift bin being $\ell_{\max} = 180$, only three multipole bins are included in the plot. To estimate the uncertainty in the E_G statistic, we employ the JK covariance matrix method, calculating the E_G values for the $N_{\rm JK} = 30$ JK subsamples used in Section 4.3. The covariance matrix of E_G is then estimated using Equation (23). For clarity, we plot the square roots of the diagonal elements of this covariance matrix as 1σ error bars on the data points in Figure 4.

We observe that the estimates of $\hat{E}_G(\ell)$ are generally consistent with the predictions of GR at 68% confidence level across most redshift bins, with no significant scale-dependent deviations. However, the E_G measurements display considerable fluctuations, suggesting that the precision of the current observational data is limited. Given that our analysis assumes the scale independence of the RSD parameter β, these fluctuations in the $\hat{E}_G(\ell)$ estimates are primarily influenced by the ratios of the power spectra. As shown in Figure 3, even within the redshift bin $0.55 < z < 0.7$, the autocorrelation power spectrum is slightly lower than the theoretical curve, and the galaxy–CMB lensing cross-correlation power spectrum deviates significantly from the theoretical model for all bins in certain band powers. In comparison with the ratio R_ℓ and $\hat{E}_G(\ell)$ in Figure 4, we find that these deviations closely correspond to the trends observed in R_ℓ and $\hat{E}_G(\ell)$ for the respective redshift bins. Specifically, the multipoles where R_ℓ and $\hat{E}_G(\ell)$ yield negative results are precisely those where $C_\ell^{g\kappa}$ also takes negative values. This suggests that the cross-correlation power spectrum between galaxies and CMB lensing is the dominant contributor to the observed fluctuations. To validate this idea, we roughly estimated the contributions to the E_G error from the three components (C_ℓ^{gg}, $C_\ell^{g\kappa}$, and β) using the error propagation formula. For simplicity, we assumed the three components to be independent, and the results indicated that the cross correlation contributes over 90% to the E_G error. Therefore, improving the precision of $\hat{E}_G(\ell)$ estimates would likely benefit significantly from more accurate measurements of the cross-correlation power spectrum $C_\ell^{g\kappa}$.

In contrast to the first three redshift bins, it is notable that the E_G results within the redshift range $0.7 < z < 0.85$ are generally lower than those predicted by the ΛCDM model, a trend that becomes more pronounced in the subsequent constant E_G estimation. However, as shown in Figure 3, the power spectra C_ℓ^{gg} and $C_\ell^{g\kappa}$ for this redshift bin align closely with theoretical predictions, suggesting that this discrepancy may be due to an overestimated β parameter. We posit that the

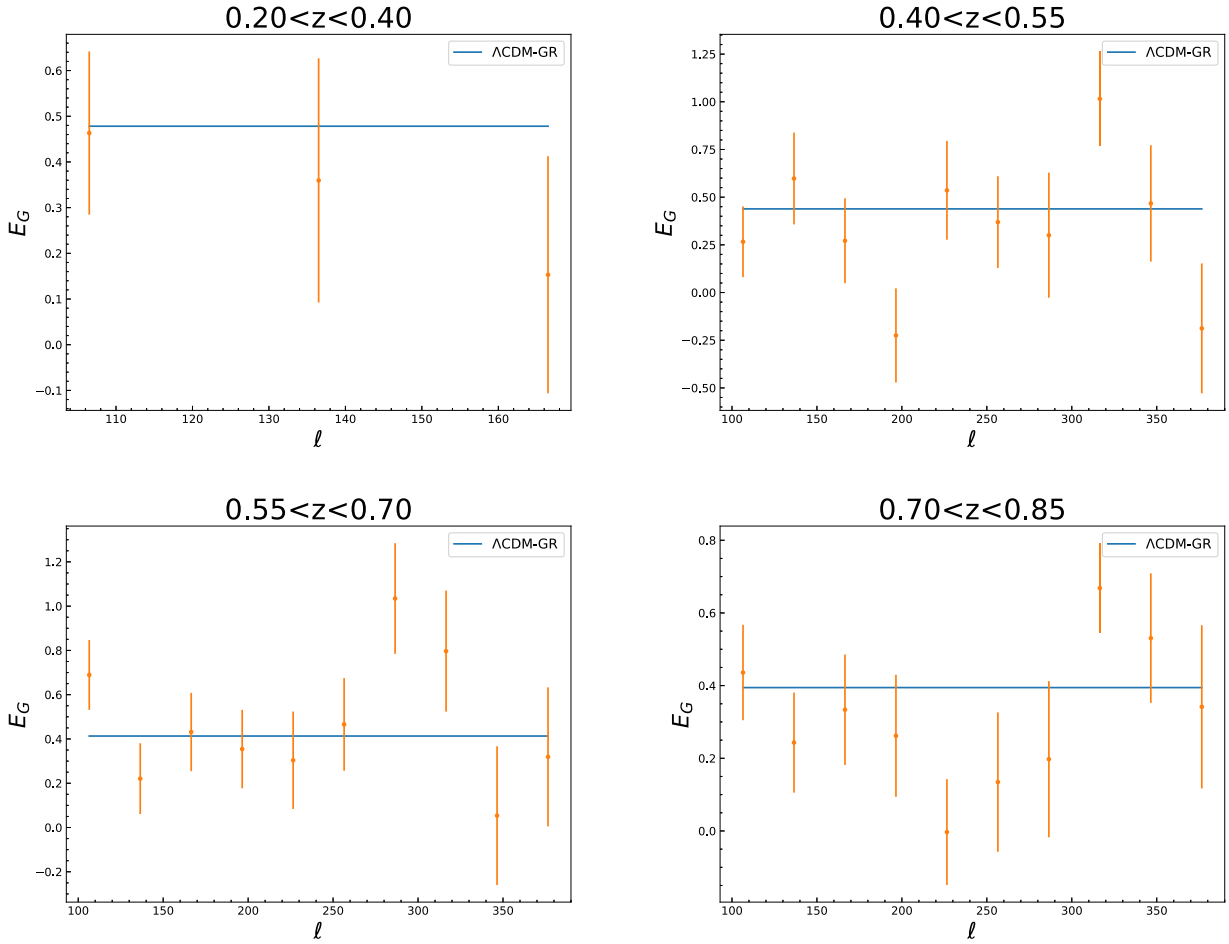

Figure 4. The estimations of the E_G statistic for the DES MagLim samples, combined with the Planck lensing measurements at the four redshift bins. The blue lines represent the theoretical prediction within the ΛCDM model, which is scale independent.

primary cause of the overestimation of $\beta(z)$ stems from the underestimation of $\hat{b}(z)$, as derived from the DES chains in the fourth redshift bin. Specifically, the best-fit value of $\hat{b}(z_4)$ is noticeably lower compared to the values obtained in the other three redshift bins. Although, in theory, E_G should be independent of galaxy bias, as this term cancels out in the calculation, this assumption holds only if C_ℓ^{gg}, $C_\ell^{g\kappa}$, and β yield consistent estimates of galaxy bias. However, these three constraints may not be fully consistent.

For instance, G. Marques et al. (2024) analyzed the constraints on galaxy bias from the autocorrelation of MagLim galaxies and their cross correlation with CMB lensing using the fourth data release of the Atacama Cosmology Telescope. Their findings indicate that, with other cosmological parameters fixed, C_ℓ^{gg} favors a higher galaxy bias than $C_\ell^{g\kappa}$, with the difference reaching 2.43σ in the $0.7 < z < 0.85$ bin. This discrepancy likely impacts the constraint on $\hat{b}$, derived from the 3×2 pt analysis, which may also be subject to such inconsistencies. Therefore, we suggest that this inconsistency could be a significant factor affecting the final E_G estimates in this redshift range.

4.5. *Scale-independent* E_G

In addition to examining the E_G statistic as a function of multipoles, we also consider the estimation of a scale-independent $\bar{E}_G$ by fitting a constant value across all scales. The best-fit value of $\bar{E}_G$ is inferred by minimizing the χ^2 function, given by

$$\chi^2 = [\hat{E}_G(\ell) - \bar{E}_G]^T \hat{\boldsymbol{C}}^{-1} [\hat{E}_G(\ell) - \bar{E}_G], \tag{28}$$

where $\hat{\boldsymbol{C}}$ denotes the estimated covariance matrix of $\hat{E}_G(\ell)$, which is also estimated using the JK resampling method. The maximum likelihood estimate for $\bar{E}_G$ can be expressed analytically, as shown in Y. Zhang et al. (2021)

$$\bar{E}_G = \frac{\sum_{\ell,\ell'} \hat{\boldsymbol{C}}_{\ell\ell'}^{-1} \hat{E}_G(\ell')}{\sum_{\ell,\ell'} \hat{\boldsymbol{C}}_{\ell\ell'}^{-1}}, \tag{29}$$

with the corresponding statistical uncertainty

$$\sigma(\bar{E}_G) = \boldsymbol{M} \times \left(\sum_{\ell,\ell'} \hat{\boldsymbol{C}}_{\ell\ell'}^{-1} \right)^{-1/2}, \tag{30}$$

where $\hat{\boldsymbol{C}}_{\ell\ell'}^{-1}$ represents the unbiased covariance matrix obtained in the previous section, and $\boldsymbol{M}$ is the correction factor introduced in Equation (26).

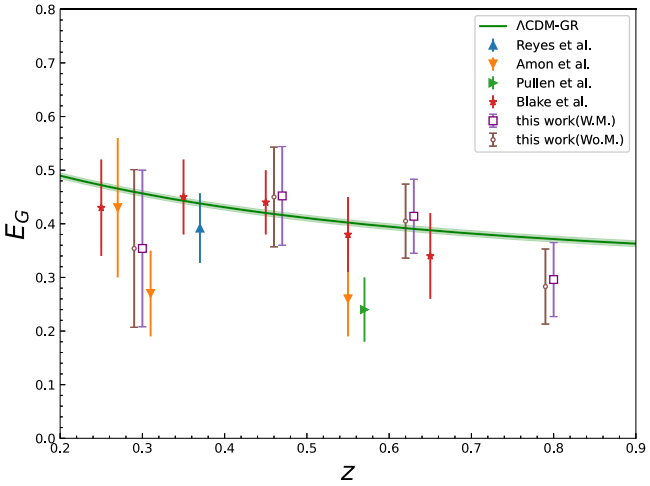

Figure 5. The scale-independent measurements of the E_G statistic for the four redshift bins of the DES MagLim sample. "W.M." and "Wo.M." represent measurements with and without the magnification bias effect, respectively. For comparison, previous E_G measurements from other studies are also shown, alongside the theoretical prediction based on the ΛCDM model (green solid line).

Finally, we obtain measurements of the scale-independent E_G in the four redshift bins at 68% confidence level

$$\begin{aligned}\bar{E}_G(z_1) &= 0.354 \pm 0.146,\\ \bar{E}_G(z_2) &= 0.452 \pm 0.092,\\ \bar{E}_G(z_3) &= 0.414 \pm 0.069,\\ \bar{E}_G(z_4) &= 0.296 \pm 0.069.\end{aligned} \tag{31}$$

In Figure 5, we present a summary of previous E_G estimates alongside the results obtained in this work, compared with the predicted values of E_G within the ΛCDM model. Our measurements show good consistency with other E_G estimates, as well as with the ΛCDM predictions. However, our results exhibit larger statistical uncertainties, particularly at lower redshifts. This is likely due to the smaller $\ell_{\rm max}$ chosen in these redshift bins, which reduces the amount of available information. Comparing different bins indicates that larger $\ell_{\rm max}$ values generally lead to smaller statistical uncertainties in E_G. However, even with increased $\ell_{\rm max}$, the errors remain too large to effectively differentiate between various MG models.

Finally, we conducted a brief analysis of the impact of magnification bias on our results. A. M. Dizgah & R. Durrer (2016) highlighted that foreground density perturbations not only magnify regions around galaxies but also alter the selection of galaxies near the observational flux limit, potentially introducing biases in galaxy clustering. In subsequent studies, S. Yang & A. R. Pullen (2018) found that the influence of magnification bias is relatively minor for most spectroscopic galaxy surveys but becomes significant in photometric galaxy surveys. To qualitatively assess this impact, we adopted the magnification bias parameters from G. Marques et al. (2024), applying values of 0.642, 0.63, 0.776, and 0.794 for the four redshift bins, respectively.

We then computed the theoretical changes in $C_\ell^{\rm gg}$, $C_\ell^{\rm g\kappa}$, and E_G with and without accounting for this magnification bias correction. Our findings suggest that the effect of magnification bias on the autocorrelation power spectrum is negligible, while its impact on the cross-correlation power spectrum increases with redshift but remains modest. The influence on E_G is most pronounced in the highest redshift bin, resulting in an average shift of approximately 4%. The results are also presented in Figure 5, with label "Wo.M." Given the current level of uncertainty in our measurements, we conclude that the effect of magnification bias can be considered negligible for this analysis.

5. Forecast

Given that the current E_G measurements derived from existing observations lack the precision required to effectively distinguish between different MG models, we now turn to an exploration of potential improvements in the estimation of E_G with upcoming LSS photometric surveys and CMB measurements. Future surveys, such as CSST, promise to significantly enhance both the quantity and quality of photometric data, offering improved galaxy-clustering measurements. Similarly, the next-generation stage-4 ground-based CMB experiment (CMB-S4) will yield more precise CMB-lensing maps, which will contribute to reducing uncertainties in the cross-correlation power spectrum.

5.1. CSST

The CSST, as part of the Chinese Space Station Optical Survey, is equipped with a 2 m aperture and seven photometric filters spanning a broad wavelength range of 255–1000 nm. These filters—near-ultraviolet, u, g, r, i, z, and y—are designed to detect point sources with 5σ magnitude limits ranging from 24.4 to 26.3 AB mag, depending on the band.

To characterize the number density distribution of galaxies in the survey, we adopt a parametric model for the galaxy distribution, $n(z)$, expressed as

$$n(z) \propto z^\alpha \exp\left[-\left(\frac{z}{z_0}\right)^\beta\right], \tag{32}$$

where the parameters α, β, and z_0 are chosen to describe the survey's galaxy population. Based on previous works like Y. Gong et al. (2019), we use $\alpha = 2$, $\beta = 1$, and $z_0 = 0.3$, which roughly match the expected distribution of galaxies for photometric surveys like the CSST.

For tomographic analysis, where galaxies are divided into several redshift bins, the number density of galaxies in a specific redshift bin i, denoted as $n_i(z)$, is derived by integrating the galaxy distribution $n(z)$ over the redshift bin limits and incorporating uncertainties from photometric redshift errors. The probability distribution of the observed redshift z_p given the true redshift z is modeled by a Gaussian distribution

$$p(z_p|z) = \frac{1}{\sqrt{2\pi}\,\sigma_z}\exp\left[-\frac{(z-z_p)^2}{2\sigma_z^2}\right], \tag{33}$$

where σ_z is the redshift scatter, typically modeled as a function of redshift. For simplicity, we assume a constant redshift scatter $\sigma_z = 0.05$, which is a reasonable approximation for future photometric surveys.

The effective galaxy distribution in a given redshift bin is then calculated using

$$n_i(z) = \frac{1}{2}n(z)\left[\mathrm{erf}\left(\frac{z_{\rm max}-z}{\sqrt{2}\,\sigma_z}\right) - \mathrm{erf}\left(\frac{z_{\rm min}-z}{\sqrt{2}\,\sigma_z}\right)\right], \tag{34}$$

where erf is the error function, and $z_{\rm min}$ and $z_{\rm max}$ represent the edges of the redshift bin. This equation accounts for the smearing effect of redshift errors, allowing us to compute the number density of galaxies within each tomographic bin.

For this analysis, we divide the survey into four uniform redshift bins, and the corresponding surface galaxy densities $\bar{n}_i$ in units of galaxies per square arcminute are assigned as 7.9, 11.5, 4.6, and 3.7 for the four bins, respectively. The galaxy bias, which affects the clustering properties of galaxies, is assumed to follow a linear relation with redshift: $b(z) = 1 + 0.84z$, as derived from previous forecasts for similar surveys (Y. Gong et al. 2019; H. Lin et al. 2022). This parameterization of galaxy bias and number density will allow for accurate predictions of galaxy clustering and cross-correlation power spectra, enabling the study of cosmological parameters such as dark energy, gravity, and the growth of LSS with the CSST.

5.2. CMB-S4

CMB-S4 (K. N. Abazajian et al. 2016; K. Abazajian et al. 2022) will be a major advancement in CMB science, equipped with dedicated telescopes featuring highly sensitive superconducting cameras. CMB-S4 is poised to push the boundaries of CMB-lensing research by producing lensing maps with significantly higher signal-to-noise ratios, thanks to its superior sensitivity and enhanced polarization capabilities. With better polarization sensitivity, CMB-S4 will generate lensing maps less affected by contamination from foregrounds, such as dust or other cosmic sources, that can obscure CMB signals. Furthermore, the experiment's multifrequency approach will aid in reducing foreground contamination in temperature, as well as polarization-based lensing estimates. Specifically, the polarization-based estimates, relying on *E*- and *B*-modes, will be the most important for CMB-S4, providing more accurate and sharper lensing maps. This will also facilitate improved cross correlation with LSS maps from next-generation galaxy surveys.

For the purposes of analysis, we model the CMB-S4 telescope beam with an FWHM of 1′ and assume white noise levels of 1 μK arcmin for temperature and 1.4 μK arcmin for polarization. The noise power spectra deconvolved with a beam, $N_\ell^{\rm TT}$ for temperature and $N_\ell^{\rm EE}$ and $N_\ell^{\rm BB}$ for polarization, are modeled as Gaussian noise, given by the expression

$$N_\ell^{\rm XX} = s_X^2 \exp\left[\ell(\ell+1)\frac{\theta_{\rm FWHM}^2}{8\log 2}\right], \tag{35}$$

where X refers to either temperature (*T*) or polarization (*E*, *B*), s_X is the polarization and temperature noises in units of μK rad, and $\theta_{\rm FWHM}$ is the beam's FWHM in radians.

For CMB-lensing reconstruction, we utilize the quadratic estimator method for the *EB* mode (*E*-mode polarization and *B*-mode lensing signal), as described by W. Hu & T. Okamoto (2002). This approach is implemented using the QUICKLENS software package, which allows for efficient estimation of lensing potentials. The combination of high sensitivity, low noise levels, and advanced reconstruction techniques in CMB-S4 will enable a dramatic improvement in lensing signal extraction, offering new insights into the underlying structure and evolution of the Universe.

Table 3
Free Parameters Considered in the Constraint Process

Parameter	Fiducial Values	Prior
$\Omega_{m,0}$	0.32	flat(0, 1)
n_s	0.9665	flat(0.7, 1)
σ_8	0.83	flat(0, 1)
h_0	0.72	flat(0.5, 1)

Note. The first column shows the names of our free parameters. The second and third columns show the fiducial values and the prior ranges of the parameters, respectively.

5.3. E_G Uncertainties

Based on the performance parameters of the CSST photometric redshift survey and the CMB-S4 lensing measurements, we estimate the uncertainties associated with the E_G statistic across four distinct redshift bins. Consistent with previous analyses, we establish a minimum multipole of $\ell_{\rm min} = 80$ and utilize the $k_{\rm nl}$ relation to determine the maximum multipoles for each of the redshift bins. Given the anticipated performance enhancements offered by the CSST, we set the cutoff scale for $\ell_{\rm max}$ at 1000. Consequently, we derive the maximum multipoles for the four redshift bins as follows: $\ell_{\rm max} = 307,\ 815,\ 1000,$ and 1000.

In our analysis, we adopt a Markov Chain Monte Carlo (MCMC) approach to enhance our estimates. The corresponding χ^2 statistic is formulated as

$$\chi^2 = \sum_\ell [\langle \boldsymbol{d}(\ell)\rangle - \boldsymbol{t}(\ell)]\,{\rm Cov}^{-1}[\langle \boldsymbol{d}(\ell)\rangle - \boldsymbol{t}(\ell)], \tag{36}$$

where $\langle \boldsymbol{d}(\ell)\rangle$ and $\boldsymbol{t}(\ell)$ represent the averaged data vectors and theoretical vectors, respectively. In this work, the averaged data vectors ($\langle\hat{C}_\ell^{\rm gg}\rangle$, $\langle\hat{C}_\ell^{\rm g\kappa}\rangle$, $\langle\hat{\beta}\rangle$) include the instrument noise, while the theoretical vectors ($C_\ell^{\rm gg}$, $C_\ell^{\rm g\kappa}$, β) are derived from the constrained parameters summarized in Table 3. The total χ^2 for our analysis is estimated as

$$\chi^2_{\rm tot} = \chi^2_{\rm gg} + \chi^2_{\rm g\kappa} + \chi^2_\beta, \tag{37}$$

where $\chi^2_{\rm gg}$, $\chi^2_{\rm g\kappa}$, and χ^2_β correspond to the contributions from photometric galaxy clustering, galaxy–CMB lensing, and the RSD parameter β, respectively.

Initially, we estimate the power spectra $C_\ell^{\rm gg}$ and $C_\ell^{\rm g\kappa}$ derived from the CSST photometric redshift survey and CMB-S4 lensing measurements, alongside the measurements of β from the CSST photometric redshift survey. Subsequently, we jointly constrain related cosmological parameters, including the current matter energy density $\Omega_{m,0}$ and the amplitude of structure growth σ_8, utilizing these measurements. Finally, we leverage the constraints on these cosmological parameters to infer the uncertainties associated with E_G at the relevant scales.

The covariance of the angular power spectra $C_\ell^{\rm gg}$ and $C_\ell^{\rm g\kappa}$ is expressed as

$$\begin{aligned}&{\rm Cov}[\tilde{C}_{\rm XY}(\ell),\,\tilde{C}_{\rm XY}(\ell')]\\ &\quad= \frac{\delta_{\ell\ell'}}{f_{\rm sky}\,\Delta\ell(2\ell+1)}[\tilde{C}_{\rm XX}(\ell)\tilde{C}_{\rm YY}(\ell) + \tilde{C}_{\rm XY}(\ell)\tilde{C}_{\rm XY}(\ell)],\end{aligned} \tag{38}$$

where $f_{\rm sky} = 0.323$ represents the fraction of the sky covered, and $\tilde{C}_{\rm XY}(\ell)$ denotes the signal of the angular power spectra

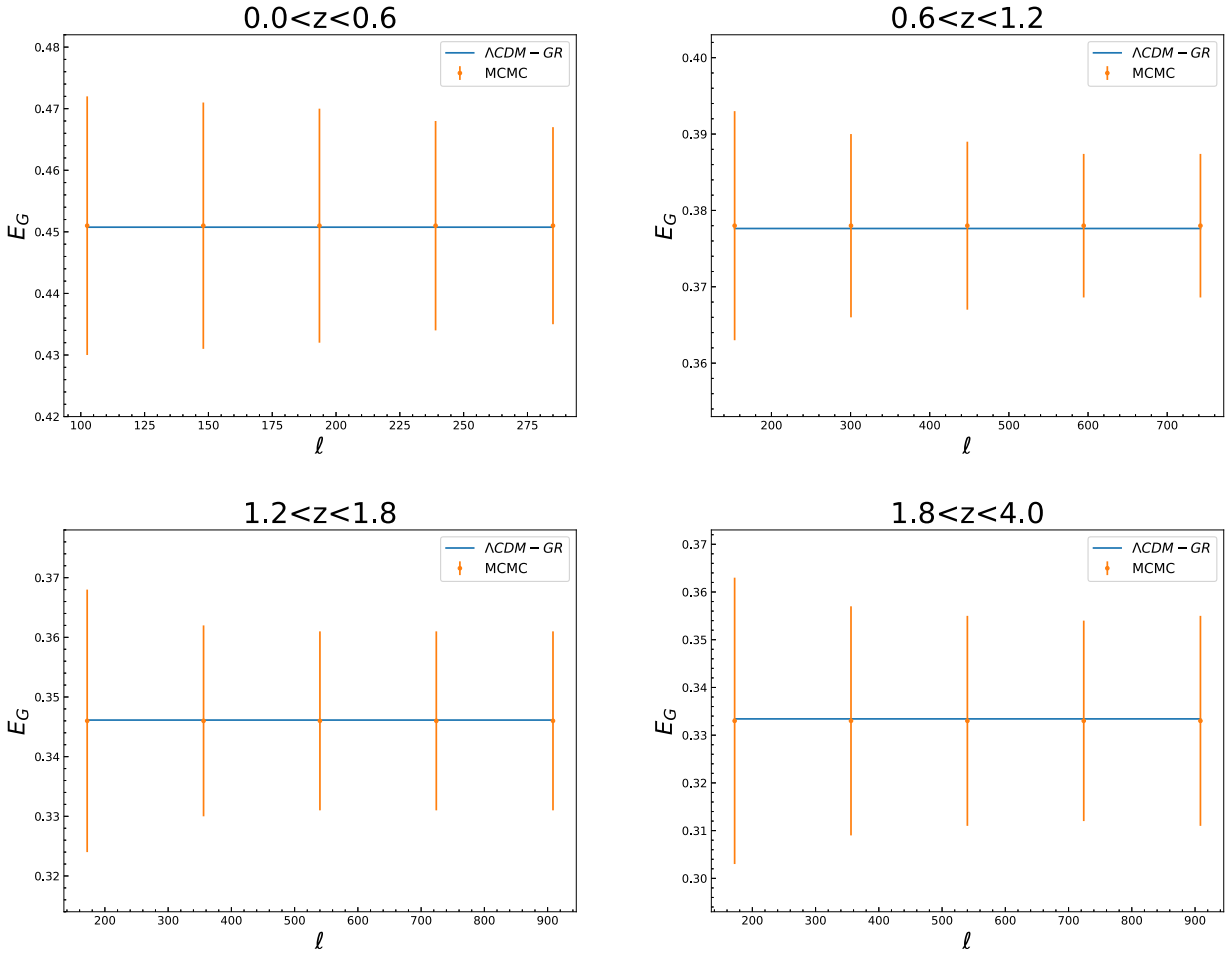

Figure 6. The estimations of the E_G statistic at redshift bins for the CSST photometric redshift survey, combined with the CMB-S4 lensing measurements. The blue lines represent the theoretical prediction within the ΛCDM model.

augmented by shot noise. Here, X and Y may refer to the same or different tracers, such as galaxies and CMB lensing. To estimate the error in the RSD parameter β for each redshift bin, we employ the relation $\sigma(\beta)/\beta = 0.085\sqrt{0.1(1+1)/(z_2 - z_1)}$ (S. Yang & A. R. Pullen 2018), where z_2 and z_1 are the upper and lower limits of the redshift distribution, respectively.

We employ the MCMC sampler from the publicly available `Cobaya` package (J. Torrado & A. Lewis 2021) to perform likelihood sampling. The convergence of the chains is assessed using the generalized version of the $R-1$ Gelman–Rubin statistic (A. Lewis 2013; A. Gelman & D. B. Rubin 1992), with convergence defined by the criterion $R - 1 < 0.01$. To mitigate the effects of initial conditions, the first 30% of the chains are discarded as burn-in. Upon obtaining constraints on the cosmological parameters, we utilize these constraints to infer the uncertainties associated with E_G at the relevant scales.

Figure 6 illustrates the estimated results of E_G as a function of multipoles for various redshift bins, demonstrating consistency with the theoretical model within the 1σ confidence interval. Notably, our estimates exhibit more than a fivefold improvement in precision compared to the photometric results obtained from the DES. Furthermore, in our estimation of the constant $\bar{E}_G$, the overall error achieved is generally at the 1% level, representing a significant enhancement over current results. According to A. R. Pullen et al. (2015), this level of precision enables the differentiation of GR from chameleon gravity (with $\beta > 1.1$) at the 5σ level, and allows for the distinction of $f(R)$ gravity from GR at the 13σ level for $B_0 > 10^{-7}$, thereby providing a stringent test of the viability of $f(R)$ theories.

Finally, we assessed the impact of magnification bias on our results. To simplify our analysis, we employed the magnification bias fitting formula derived from the Flagship simulations of the Euclid mission (F. Lepori et al. 2022), which has performance characteristics similar to those of the CSST. The fitting formula is expressed as

$$s(z) = s_0 + s_1 z + s_2 z^2 + s_3 z^3, \tag{39}$$

where the coefficients are defined as $s_0 = 0.0842$, $s_1 = 0.0532$, $s_2 = 0.298$, and $s_3 = -0.0113$. Our findings indicate that the presence of magnification bias could lead to deviations of up to 6% in estimates of E_G. This magnitude of bias is significant and should be taken into account for future high-precision estimates of E_G. Consequently, we emphasize that magnification bias must be carefully addressed in subsequent analyses to ensure that the results accurately reflect the underlying gravitational theory.

6. Conclusions

The E_G statistic, which integrates gravitational lensing and LSS, represents a valuable cosmological probe for testing theories of gravity, particularly because it is independent of

galaxy bias and σ_8. Unlike traditional methods relying on spectroscopic surveys, this study estimates E_G at four effective redshifts, utilizing photometric redshift data from the DES MagLim sample alongside Planck 2018 CMB-lensing convergence maps. To address the significant redshift uncertainties inherent in photometric redshift surveys, we adopt a novel approach for estimating the RSD parameter $\beta = \hat{f}/\hat{b}$, where $\hat{f} = f\sigma_8$ and $\hat{b} = b\sigma_8$.

For the growth rate parameter $\hat{f}$, we compile current measurements from various LSS spectroscopic redshift surveys and implement an ANN algorithm, `ReFANN`, to derive estimates. The ANN-based predictions for $\hat{f}$ demonstrate consistency with the standard ΛCDM model at the 68% confidence level.

For the linear bias parameter $\hat{b}$, we utilize constraints on $b(z)$ and $\sigma_8(z)$ across four redshift bins provided by the DES collaboration to derive the corresponding $\hat{b}(z)$ values. However, the derived value of $\hat{b}$ for the highest redshift bin ($z = 0.8$) is notably low, potentially introducing systematic uncertainties in the final E_G measurements.

We estimate the E_G statistic by analyzing the angular power spectra C_ℓ^{gg} and $C_\ell^{g\kappa}$. Our results for $E_G(\ell)$ reveal no significant scale dependence across all redshift bins. Moreover, we present new measurements of the E_G statistic: $E_G = 0.354 \pm 0.146$, 0.452 ± 0.092, 0.414 ± 0.069, and 0.296 ± 0.069 (68% confidence limit) for redshifts $z = 0.30$, 0.47, 0.63, and 0.80, respectively. These estimates are generally consistent with other E_G measurements and predictions from ΛCDM, though the statistical uncertainties remain relatively large. Additionally, the E_G measurement in the fourth redshift bin is notably lower than the theoretical prediction, likely due to an underestimation of the bias in the DES sample at this redshift.

Given the substantial uncertainties in current observational data, we simulate future data from the forthcoming CSST and CMB-S4 experiment to project potential improvements in E_G precision. Our simulations indicate that future surveys could reduce the uncertainties in E_G measurements to the 1% level, enabling a definitive distinction between GR and various MG models.

Lastly, we assess the impact of magnification bias on the E_G estimates. Our findings suggest that magnification bias could introduce deviations of up to 6% in the E_G measurements. This level of bias is significant, and we underscore the importance of carefully accounting for magnification bias in future high-precision E_G analyses to ensure the accuracy and reliability of constraints on gravitational theories.

Acknowledgments

This work is supported by the National Natural Science Foundation of China, under grant Nos. 12473004 and 12021003, the National Key R&D Program of China, No. 2020YFC2201603, the China Manned Space Program through its Space Application System, and the Fundamental Research Funds for the Central Universities.

References

Abazajian, K., Abdulghafour, A., Addison, G. E., et al. 2022, arXiv:2203.08024
Abazajian, K. N., Adshead, P., Ahmed, Z., et al. 2016, arXiv:1610.02743
Abbott, T., Aguena, M., Alarcon, A., et al. 2023, PhRvD, 107, 083504
Abbott, T. M., Aguena, M., Alarcon, A., et al. 2022, PhRvD, 105, 023520
Aghanim, N., Akrami, Y., Ashdown, M., et al. 2020, A&A, 641, A8
Alam, S., Ata, M., Bailey, S., et al. 2017b, MNRAS, 470, 2617
Alam, S., Miyatake, H., More, S., Ho, S., & Mandelbaum, R. 2017a, MNRAS, 465, 4853
Amon, A., Blake, C., Heymans, C., et al. 2018, MNRAS, 479, 3422
Beutler, F., Blake, C., Colless, M., et al. 2012, MNRAS, 423, 3430
Beutler, F., Seo, H.-J., Saito, S., et al. 2017, MNRAS, 466, 2242
Blake, C., Amon, A., Asgari, M., et al. 2020, A&A, 642, A158
Blake, C., Brough, S., Colless, M., et al. 2012, MNRAS, 425, 405
Blake, C., Baldry, I. K., Bland-Hawthorn, J., et al. 2013, MNRAS, 436, 3089
Blake, C., Joudaki, S., Heymans, C., et al. 2016, MNRAS, 456, 2806
Chisari, N. E., Alonso, D., Krause, E., et al. 2019, ApJS, 242, 2
Chuang, C.-H., Prada, F., Pellejero-Ibanez, M., et al. 2016, MNRAS, 461, 3781
Chuang, C.-H., & Wang, Y. 2013, MNRAS, 435, 255
Davis, M., Nusser, A., Masters, K. L., et al. 2011, MNRAS, 413, 2906
De La Torre, S., Guzzo, L., Peacock, J., et al. 2013, A&A, 557, A54
De La Torre, S., Jullo, E., Giocoli, C., et al. 2017, A&A, 608, A44
De Vicente, J., Sánchez, E., & Sevilla-Noarbe, I. 2016, MNRAS, 459, 3078
Dizgah, A. M., & Durrer, R. 2016, JCAP, 2016, 035
Dodelson, S., & Schneider, M. D. 2013, PhRvD, 88, 063537
Feix, M., Branchini, E., & Nusser, A. 2017, MNRAS, 468, 1420
Feix, M., Nusser, A., & Branchini, E. 2015, PhRvL, 115, 011301
Flaugher, B., Diehl, H., Honscheid, K., et al. 2015, AJ, 150, 150
Garcìa-Garcìa, C., Ruiz-Zapatero, J., Alonso, D., et al. 2021, JCAP, 2021, 030
Gelman, A., & Rubin, D. B. 1992, StaSc, 7, 457
Giannantonio, T., Fosalba, P., Cawthon, R., et al. 2016, MNRAS, 456, 3213
Gil-Marìn, H., Guy, J., Zarrouk, P., et al. 2018, MNRAS, 477, 1604
Gil-Marìn, H., Percival, W. J., Verde, L., et al. 2017, MNRAS, 465, 1757
Gong, Y., Liu, X., Cao, Y., et al. 2019, ApJ, 883, 203
Hartlap, J., Simon, P., & Schneider, P. 2007, A&A, 464, 399
Hawken, A., Granett, B., Iovino, A., et al. 2017, A&A, 607, A54
Hivon, E., Górski, K. M., Netterfield, C. B., et al. 2002, ApJ, 567, 2
Hou, J., Sánchez, A. G., Scoccimarro, R., et al. 2018, MNRAS, 480, 2521
Howlett, C., Ross, A. J., Samushia, L., Percival, W. J., & Manera, M. 2015, MNRAS, 449, 848
Howlett, C., Staveley-Smith, L., Elahi, P. J., et al. 2017, MNRAS, 471, 3135
Hu, W., & Okamoto, T. 2002, ApJ, 574, 566
Hudson, M. J., & Turnbull, S. J. 2012, ApJL, 751, L30
Huterer, D., Shafer, D. L., Scolnic, D. M., & Schmidt, F. 2017, JCAP, 2017, 015
Icaza-Lizaola, M., Vargas-Magaña, M., Fromenteau, S., et al. 2020, MNRAS, 492, 4189
Kazantzidis, L., & Perivolaropoulos, L. 2018, PhRvD, 97, 103503
Lepori, F., Tutusaus, I., Viglione, C., et al. 2022, A&A, 662, A93
Lewis, A. 2013, PhRvD, 87, 103529
Limber, D. N. 1953, ApJ, 117, 134
Lin, H., Gong, Y., Chen, X., et al. 2022, MNRAS, 515, 5743
Lyke, B. W., Higley, A. N., McLane, J., et al. 2020, ApJS, 250, 8
Marques, G., & Bernui, A. 2020, JCAP, 2020, 052
Marques, G., Madhavacheril, M., Darwish, O., et al. 2024, JCAP, 2024, 033
Mohammad, F., Bianchi, D., Percival, W., et al. 2018b, A&A, 619, A17
Mohammad, F., Granett, B. R., Guzzo, L., et al. 2018a, A&A, 610, A59
Nadathur, S., Carter, P. M., Percival, W. J., Winther, H. A., & Bautista, J. E. 2019, PhRvD, 100, 023504
Omori, Y., Giannantonio, T., Porredon, A., et al. 2019, PhRvD, 100, 043501
Okumura, T., Hikage, C., Totani, T., et al. 2016, PASJ, 68, 38
Percival, J. W., W., J., Ross, A. J., Sánchez, A. G., et al. 2014, MNRAS, 439, 2531
Perenon, L., Martinelli, M., Ilić, S., et al. 2021, PDU, 34, 100898
Pezzotta, A., de La Torre, S., Bel, J., et al. 2017, A&A, 604, A33
Porredon, A., Crocce, M., Elvin-Poole, J., et al. 2022, PhRvD, 106, 103530
Pullen, A. R., Alam, S., He, S., & Ho, S. 2016, MNRAS, 460, 4098
Pullen, A. R., Alam, S., & Ho, S. 2015, MNRAS, 449, 4326
Qin, F., Howlett, C., & Staveley-Smith, L. 2019, MNRAS, 487, 5235
Reyes, R., Mandelbaum, R., Seljak, U., et al. 2010, Natur, 464, 256
Rodrìguez-Monroy, M., Weaverdyck, N., Elvin-Poole, J., et al. 2022, MNRAS, 511, 2665
Samushia, L., Percival, W. J., & Raccanelli, A. 2012, MNRAS, 420, 2102
Sánchez, A. G., Montesano, F., Kazin, E. A., et al. 2014, MNRAS, 440, 2692
Sánchez, J., Omori, Y., Chang, C., et al. 2022, MNRAS, 522, 3163
Shi, F., Yang, X., Wang, H., et al. 2018, ApJ, 861, 137
Skara, F., & Perivolaropoulos, L. 2020, PhRvD, 101, 063521
Song, Y.-S., & Percival, W. J. 2009, JCAP, 2009, 004
Tojeiro, R., Percival, W. J., Brinkmann, J., et al. 2012, MNRAS, 424, 2339

Torrado, J., & Lewis, A. 2021, JCAP, 2021, 057
Turnbull, S. J., Hudson, M. J., Feldman, H. A., et al. 2012, MNRAS, 420, 447
Wang, G.-J., Ma, X.-J., Li, S.-Y., & Xia, J.-Q. 2020, ApJS, 246, 13
Wang, Y., Zhao, G.-B., Chuang, C.-H., et al. 2018, MNRAS, 481, 3160
Wenzl, L., Bean, R., Chen, S.-F., et al. 2024, PhRvD, 109, 083540
Wilson, M. J. 2016, arXiv:1610.08362
Yang, S., & Pullen, A. R. 2018, MNRAS, 481, 1441
Zhang, P., Liguori, M., Bean, R., & Dodelson, S. 2007, PhRvL, 99, 141302
Zhang, Y., Pullen, A. R., Alam, S., et al. 2021, MNRAS, 501, 1013
Zhao, G.-B., Wang, Y., Saito, S., et al. 2019, MNRAS, 482, 3497